Reduction kinetics of cold-bonded briquette prepared from return fines of sinter with carbon monoxide and coke

Ying Li[1], Jie Ren[1], Han Wei[1], Inam Ullah Khan[1], Mamdouh Omran[2], Timo Fabritius[2], Qifeng Shu[2], Chuan Wang[3,4], Yonggang Zang[5,6] and Yaowei Yu[1,*]

1. State Key Laboratory of Advanced Special Steel, Shanghai Key Laboratory of Advanced Ferrometallurgy, School of Materials Science and Engineering, Shanghai University, 99 Shangda Rd, Shanghai 200444, China;
2. Process Metallurgy Research Group, Faculty of Technology, University of Oulu, Oulu 90014, Finland;
3. Swerim AB, SE-971 25 Lulea, Sweden;
4. KTH Royal Institute of Technology, Material Science and Engineering, SE-100 44 Stockholm, Sweden;
5. School of Materials and Metallurgy, Guizhou University, Guiyang 550025, China;
6. Guizhou Province Key Laboratory of Metallurgical Engineering and Energy Process Saving, Guiyang 550025, China

* Corresponding author: Yaowei Yu, email: yaoweiyu@shu.edu.cn

This article has been accepted for publication and undergone full peer review but has not been through the copyediting, typesetting, pagination and proofreading process, which may lead to differences between this version and the Version of Record. Please cite this article as doi: 10.1002/srin.202300057.

Abstract

The reduction kinetics of cold-bonded briquette prepared from return fines of sinter was studied. The results revealed that cold-bonded briquettes with coke (CBBC) have a higher reduction velocity index (RVI) value than cold-bonded briquettes without coke (CBB). Interfacial chemical reaction controls the early stages of the CBB reduction process at 900 and 950 °C, followed by both interfacial chemical reaction and internal diffusion. At 1000, 1050, and 1100 °C, the early and final stages of the CBB reduction process are controlled by interfacial chemical reaction and internal diffusion respectively, while both interfacial chemical reaction and internal diffusion control middle stage. The apparent activation energies of the different stages are 46.20, 56.74, 38.24 and 40.74 kJ/mol, respectively. The gasification of carbon reaction controls the reduction process of CBBC, and the apparent activation energy is 32.42 kJ/mol. According to the results of the Friedman method, the apparent activation energy of CBB and CBBC is reasonable. Coke promotes the phase transformation in CBBC. SEM results show that the CBBC sample is more fully reduced than the CBB sample and that it has smoother corners and edges of the iron bearing phase or the metallic iron phase than the CBB sample.

Keywords: Cold-bonded briquette, return fines of sinter, kinetic analysis, phase transformation, reduction behavior

1. Introduction

Return fines of sinter is now being utilized in blast furnaces straight after cold briquetting, a novel method of return fines utilization.[1-4] This technique can prevent return fines from being repeatedly sintered at high temperatures. On the one hand, it can lower the amount of energy used by the sinter plant, and on the other, it can increase the output of the sintering process. The compressive strength, reduction degradation index, and reducibility index of cold-bonded briquette prepared from return fines are close to those of the sinter, which is acceptable for use in a large blast furnace. Cold-bonded briquette prepared from return fines has successfully substituted 5-10% of the sinter in a 2800 m^3 blast furnace in Gansu Province, China.[3, 4] However, the lack of knowledge regarding the cold-bonded briquette prepared from return fines' reduction kinetics in the blast furnace prevents further advancements in the cold-bonded briquette prepared from return fines' utilization ratio.

Numerous studies have investigated the reduction kinetics of sinter under varying conditions. The sinter's porosity, particle size, and chemical composition affect its reduction kinetics.[5] For instance, sinter with greater porosity or with a large number of microscopic pores is usually reduced more quickly because the pores enable the reducing gas to reach the reaction's interface. However, macropores (>0.125 mm) are more crucial than micropores for the increased reduction rate of sinter because the reduction front of fine pores (<0.125 mm) is complex and irregular.[6] The reduction rate usually increases with the decreasing particle size of the sinter, and varied iron oxide particle sizes result in distinct rate-controlling steps.[7] When the particle size of the sinter increases, the diffusion distance of the reducing gas increases, and the pore diffusion resistance becomes important; when decreasing the reduction temperature, the impact of particle size on the reduction rate decreases.[8] Although it could be broadly classified into the effects of iron oxide mineralogy and gangue on reduction performance, the influence of chemical composition on the reduction performance of sinter is quite complicated.[9, 10] Hematite has a higher reduction rate than monocalcium ferrite ($CaFe_2O_4$) and dicalcium ferrite ($Ca_2Fe_2O_5$), but magnetite has lower reducibility than both of these minerals.[11] Typical iron oxide gangues are SiO_2, CaO, MgO and Al_2O_3. The basicity of sinter is the ratio of CaO to SiO_2. Much research has been conducted to study the effect of basicity on the reduction of sinter,

and it has been found that increasing basicity properly can increase the reduction rate.[12-14] The effect of MgO and Al_2O_3 on the reduction behavior of sinter under certain conditions is investigated. For example, the reducibility of low silica sinter and high silica sinter decreased with increase MgO addition due to the increase in magnetite/magnesio spinel phase and silicate/slag phase.[15] At the initial stage of the non-isothermal reduction process, Al_2O_3 enhances the reduction rate up to 1073 K, and the reduction rate rises with increasing Al_2O_3 content up to 2.5%. Due to the presence of primary low melt slag including alumina, the reduction rate was noticeably slower at temperatures above 1073 K.[16] However, the porosity, particle size, and chemical composition of the cold-bonded briquette prepared from return fines are different from those of the sinter due to the briquetting process. As a result, the cold-bonded briquette's reduction kinetics are different from those of sinter due to its significantly different physicochemical features from those of sinter. There is limited information for studying the reduction kinetics of cold-bonded briquette prepared from return fines. A deep understanding of the reaction kinetics and mechanism is required for the development and effective process control of the technology of cold-bonded briquette prepared from return fines.

Our previous study found that the reducibility of cold-bonded briquette prepared from return fines was lower than that of sinter due to its large particle size, and adding coke can significantly increase reducibility.[4] Therefore, in this paper, there are two different types of samples involved in the reduction mechanism investigation, one is the cold-bonded briquette without coke (CBB), and the second one is the cold-bonded briquette with coke (CBBC). First, the reduction degree and reduction velocity index are analyzed. Subsequently, the rate-controlling steps of the reduction reaction process and activation energy are studied. Finally, the phase transformation and morphology after reduction are investigated.

2. Experimental methodology

2.1 Experimental materials

Return fines are provided by Baosteel Group Shanghai Meishan Co., Ltd. The chemical compositions and particle size distributions of the return fines are shown in Table 1 and Table 2 respectively. Figure 1 shows the x-ray diffraction pattern (XRD) of the return fines. The XRD shows that the mineral compositions of return fines are complicated, the major crystalline phases are hematite, calcium ferrite (CaFe2O4), magnetite, calcium silicate (Ca2SiO4) and fayalite (Fe2SiO4). Nut coke is also used in this study, and ultimate and proximate analysis of the coke is shown in Table 3.

Table 1 Chemical compositions of return fines (wt.%)

Constituents	TFe	FeO	CaO	SiO_2	Al_2O_3	MgO	Mn	P	S
%	57.96	8.86	9.28	4.98	1.78	1.37	0.18	0.06	0.01

Table 2 Particle size distributions of return fines (wt.%)

Particle size (mm)	<0. 5	0.5 to 2	2 to 3.15	3.15 to 5	5 to 6.3	>6.3

%	1.05	23.92	21.47	41.15	10.14	2.11

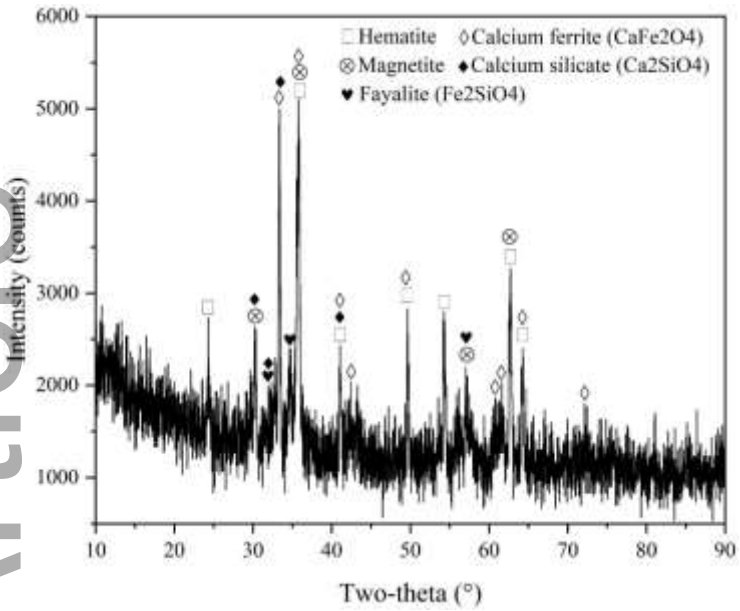

Fig. 1 X-ray diffraction pattern of return fines

Table 3 Ultimate and proximate analysis of coke (wt.%)

Fixed C	Ash	Volatiles	Moisture	S
84.70	13.20	1.70	0.40	0.6

To increase the strength of CBB, a compound binder (with an approximate 1:16 ratio of organic binder to inorganic binder) is utilized in this study. Table 4 displays the chemical analysis of the inorganic and organic components of the compound binder.

Table 4 Chemical composition of compound binder (wt.%)

Inorganic binder	CaO	SiO_2	Al_2O_3	Fe_2O_3	MgO	SO_3
	53.01	27.35	7.12	2.55	4.61	3.15
Organic binder	C	H	O	S		
	41.80	7.13	50.98	0.09		

2.2 Experimental method

2.2.1 Preparation of CBB and CBBC

In this study, two types of cold-bonded briquettes were prepared, one is CBB, and the other one is CBBC. CBB comprised 93 wt.% of return fines and 7 wt.% of the compound binder. CBBC comprised 84 wt.% of return fines, 7 wt.% of compound binder and 9 wt.% of nut coke. According to our previous studies, the amount of binder and

coke nut added is set at 7% and 9%, respectively, to ensure that the cold-bonded briquette's strength and reducibility satisfy the demands of a blast furnace[4]. The nut coke is ground to a fineness of less than 0.5 mm to ensure it is entirely utilized. A 9 wt.% of water was added in the mixing process (water content = the mass of water/(the mass of compound binder + the mass of return fines)×100%). A twin-roller machine with a briquetting pressure of 500 kg/cm^2 was used to prepare lenticular CBB and CBBC with dimensions of Φ40 mm×20 mm and a mass of about 45 g. Following a 14-day period of curing at room temperature, the CBB and CBBC were dried for 12 hours in a drying oven at 130 °C.

2.2.2 Reduction experiments

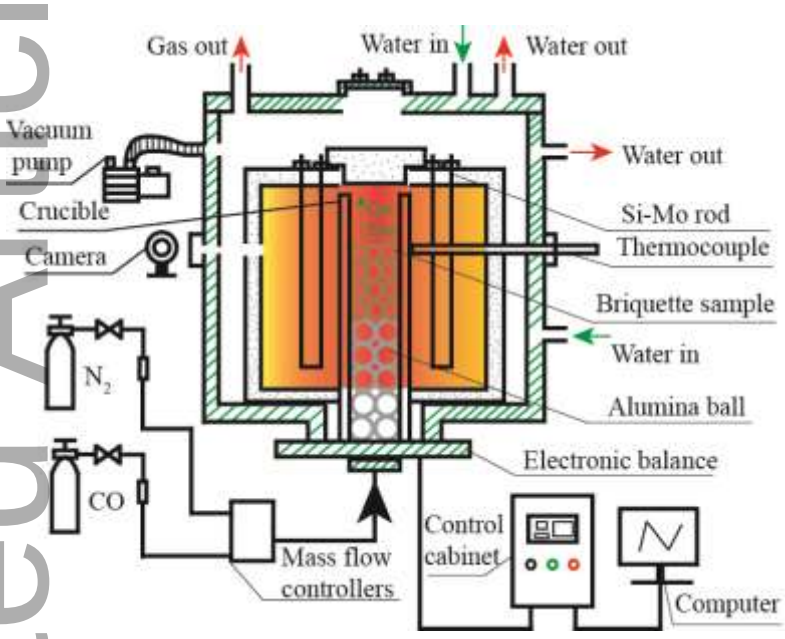

Fig. 2 Schematic diagram of reduction experimental equipment

Figure 2 depicts the schematic diagram of the experimental reduction equipment utilized in this study. The reduction procedures are summarized as follows: First, a quantitative of CBBs (or CBBCs) were filled in the crucible; Second, the CBBs (or CBBCs) were firstly preheated to the reaction temperature under N_2 atmosphere (1 L/min) untill the temperature stabilized; Third, the N_2 was changed to the reducing gas and kept reacted for 270 min, the mass of the CBBs (or CBBCs) was automatically recorded by an electronic mass balance and the computer system; Finally, the reducing gas was switched back to N_2 (1 L/min) until the crucible was cooled to room temperature to prevent the product from being re-oxidized. Five CBBs (or CBBCs) were loaded per trial at a reducing gas flow rate of 3 L/min (N_2: 50%, CO: 50%).

The reduction degree of CBB, *R*, is calculated using the following equation[17, 18]:

$$R=\left[\frac{0.111w_1}{0.430w_2}+\frac{m_1-m_t}{m_0\times 0.430w_2}\times 100\right]\times 100\% \quad (1)$$

where w_1 is the content of FeO content in the CBB, %; m_1 is the initial mass of the CBB, alumina ball and crucible, g; m_t is the mass of CBB, alumina ball and crucible at time t, g; w_2 is the content of TFe in the CBB, %; and m_0 is the initial mass of CBB, g.

The reduction degree of CBBC, α, is calculated using the following equation[19, 20]:

$$\alpha=\frac{w_0-w_t}{w_{Fe}+w_C} \quad (2)$$

where w_0 is the initial mass of sample, g; w_t is the mass of sample at reduction time t, g; w_{Fe} is the maximum

mass loss of iron oxide, g; and w_C is the maximum mass loss of coke, g.

2.2.3 Characterization

Selected samples from CBBs and CBBCs were mounted in epoxy resin, polished, and then given a platinum coating. Scanning electron microscopy (SEM, ULTRA Plus, ZEISS, Germany) was used to observe the selected CBB (and CBBC) samples. Representative parts from CBBs and CBBCs were finely grinding in an agate mortar with particle sizes less than 75 μm. The powdered CBB and CBBC samples were used for phase identification by X-ray diffraction (XRD, Ultima IV, Rigaku, Japan). The compressive strength was performed on a universal testing machine (UTM, C45.305, MTS, Eden Prairie, MN, USA) and in accordance with the method of National Standard of the People's Republic of China (GB/T 14201-93).

2.3 Kinetic analysis

2.3.1 Kinetic model of CBB

The reduction of the CBB proceeds topochemically according to the previous studies, in which the core-shrinking model is widely used to analyze the reduction process.[21-25] The core-shrinking model is applied to study the reduction kinetics of CBB in this study, and it can be expressed as follows:[18, 26]

$$M(g)+N(s)=P(g)+Q(s) \quad (3)$$

$$t=\frac{r_0\rho R}{(C_M^0-C_M^q)k_g}+\frac{Kr_0\rho}{k(1+K)(C_M^0-C_M^q)}\left[1-(1-R)^{\frac{1}{3}}\right]+\frac{r_0^2\rho}{6D_e(C_M^0-C_M^q)}[1-3(1-R)^{\frac{2}{3}}+2(1-R)] \quad (4)$$

where M(g), N(s), P(g), and Q(s) are the gas reactant, the solid reactant, the gas products, and the solid products, respectively. Where R is the reduction degree, %; t is the reduction time, s; r_0 is the initial equivalent radius of CBB, m; ρ is the oxygen concentration of CBB, mol/m^3; C_M^0 is the initial concentration of reduction gas, mol/m^3; C_M^q is the equilibrium concentration of reduction gas, mol/m^3; k_g is the mass transfer coefficient of reduction gas in the gas-film, ms^{-1}; K is the equilibrium constant for chemical reaction; k is the rate constants for chemical reactions, m/s; De is the effective diffusion coefficient of reduction gas, m^2/s.

The experiment's gas flow rate exceeded the critical flow rate, and external diffusion is typically quicker than interfacial chemical reaction and internal diffusion.[24] Therefore, Eq. (4) can be expressed by the following equation

$$t=\frac{Kr_0\rho}{k(1+K)(C_M^0-C_M^q)}\left[1-(1-R)^{\frac{1}{3}}\right]+\frac{r_0^2\rho}{6D_e(C_M^0-C_M^q)}[1-3(1-R)^{\frac{2}{3}}+2(1-R)] \quad (5)$$

When the overall rate is controlled by the chemical reaction at the interface, the kinetics equation is expressed as Eq. (6),

$$t=\frac{Kr_0\rho}{k(1+K)(C_M^0-C_M^q)}\left[1-(1-R)^{\frac{1}{3}}\right] \quad (6)$$

Based on Eq. (6), plotting $1-(1-R)^{\frac{1}{3}}$ vs. t and making a linear fitting, k can be calculated by the slope.

When the overall rate is controlled by the mix of chemical reaction at the interface and inner diffusion, the kinetics equations are expressed as Eq. (7),

$$\frac{t}{F}=t_d\left[3F-2F^2\right]+t_c \quad (7)$$

Eqs. (8), (9), and (10) presents the t_c, t_d and F, respectively:[18, 26]

$$t_c=\frac{Kr_0\rho}{k(1+K)(C_M^0-C_M^q)} \quad (8)$$

$$t_d=\frac{r_0^2\rho}{6D_e(C_M^0-C_M^q)} \quad (9)$$

$$F=1-(1-R)^{\frac{1}{3}} \quad (10)$$

Plotting $\frac{t}{F}$ vs. $3F-2F^2$ and making a linear fitting, slope and intercept correspond to the t_d and t_c respectively. The values of k and De can be calculated according to Eqs. (8) and (9), respectively.

According to Eq. (3), Eq. (11), and (12) can be obtained:

$$C_M^q + C_P^q = C_M^0 \quad (11)$$

$$\frac{C_P^q}{C_M^q} = K \quad (12)$$

Where C_P^q is the equilibrium concentration of gas product P. Combining Eq. (11) and (12), Eq. (8) and Eq. (9) are change to Eq. (13) and Eq. (14),

$$t_c=\frac{r_0\rho}{kC_M^0} \quad (13)$$

$$t_d=\frac{r_0^2\rho(1+K)}{6D_eC_M^0K} \quad (14)$$

where $C_{M\,(900\,℃)}^0 = 10.39\ mol/m^3$, $C_{M\,(950\,℃)}^0 = 9.97\ mol/m^3$, $C_{M\,(1000\,℃)}^0 = 9.57\ mol/m^3$, $C_{M\,(1050\,℃)}^0 = 9.21\ mol/m^3$, $C_{M\,(1100\,℃)}^0 = 8.87\ mol/m^3$, $r_0 = 2\times10^{-2}m$, ρ=4570.29 mol/m^3.

When the overall rate is controlled by the inner diffusion, the kinetics equations are expressed as Eq. (15),

$$t=\frac{r_0^2\rho}{6D_e(C_M^0-C_M^q)}[1-3(1-R)^{\frac{2}{3}}+2(1-R)] \quad (15)$$

Based on Eq. (15), plotting $1-3(1-R)^{\frac{2}{3}}+2(1-R)$ vs. t and making a linear fitting, De can be calculated using the slope.

2.3.2 Kinetic model of CBBC

The CBBC sample contains coke, which makes its reduction process different from CBB. Previous studies suggested that the reduction process of CBBC may be controlled by the following steps: gasification reaction of carbon, interfacial reduction reaction, and gas diffusion through the reduction product layer.[27, 28] These rate-limiting steps can be described by the following kinetic equations respectively:[29-32]

$$-\ln(1-\alpha) = kt \quad (16)$$

$$1-(1-\alpha)^{1/3} = kt \quad (17)$$

$$[1-(1-\alpha)^{1/3}]^2 = kt \quad (18)$$

In Eqs. (16) - (18): α is the reduction degree, k is the rate constant of reaction, s^{-1}, t is the reduction time, s.

To assess the fitting effect, the results of each model were calculated and compared with the experimental results. The reduction degree of the calculation results (α_{calc}) and the experimental results (α_{exp}) were compared using mean deviation (MD) and root-mean square deviation (RMSD). The formula for calculating MD and RMSD is as

follows:[27, 33]

$$MD = \frac{\sum(\alpha_{calc}-\alpha_{exp})}{n} \quad (19)$$

$$RMSD = \sqrt{\frac{\sum(\alpha_{calc}-\alpha_{exp})^2}{n-1}} \quad (20)$$

where α_{calc} is the calculated values of the reduction degree using different models, and α_{exp} is the experimental values of the reduction degree.

2.3.3 Determining methods of apparent activation energy

To obtain the accurate activation energy value, the activation energy is calculated using two different approaches. One method is model-fitting analysis, which is based on the reaction rate constants obtained by different kinetic models; the Eq. (21) was used in this analysis. The activation energy can be obtained from the slope of the plots of lnk versus 1/T. The other method is Friedman analysis, which is the model-free (isoconversional) method of kinetic analysis that calculates activation energy at different conversion degrees, the equation is shown in Eq. (22).[34-36] Friedman analysis is used to test whether the activation energy obtained by the model fitting analysis is within a reasonable range. For a constant value of conversion degree α, the activation energy can be obtained from the slope of plots of ln(dα/dt) versus 1/T.

$$lnk = lnA - \frac{E_a}{RT} \quad (21)$$

$$ln\frac{d\alpha}{dt} = lnAf(\alpha) - \frac{E_a}{RT} \quad (22)$$

where Ea is the activation energy, kJ/mol, A is the frequency factor, s^{-1}, T is the temperature, K, and f(α) is an unknown conversion function.

3. Results and discussion

3.1 Reduction degree and RVI

The CBBs and CBBCs were isothermally reduced with CO and the kinetic results are shown in Figure 3 (a) and 3 (b), respectively. This experiment was carried out under the condition with 50 ℃ intervals ranging from 900 ℃ to 1100 ℃. Figure 3 shows that the reduction degree of CBB and CBBC increased with the increase of reduction temperature. The reduction degree is 71.16%, 76.32%, 82.37%, 86.65% and 90.43% after the CBBs are reduced at 900 ℃, 950℃,1000 ℃,1050 ℃ and 1100 ℃, respectively, for 270 min. The reduction degrees are 78.06%, 80.72%, 84.14%, 86.70% and 89.11% after the CBBCs are reduced at 900 ℃, 950℃,1000 ℃,1050 ℃ and 1100 ℃, respectively, for 270 min. It demonstrates that CBB and CBBC reduction degree is significantly influenced by reduction temperature. More mineral phase transformations occur as the temperature rises, resulting in more cracks. These cracks open the closed pores while also serving as channels for the diffusion of reducing gas, which ultimately improves kinetic conditions.[24] Therefore, the reduction degree was apparently accelerated as the temperature increased. By changing the porosity, the raw materials' particle size significantly affects the reduction kinetics. The uniform particle size distribution is managed during the sample preparation process through the process of mixing. The impact of the particle size of raw materials on the reduction kinetics will not be discussed.

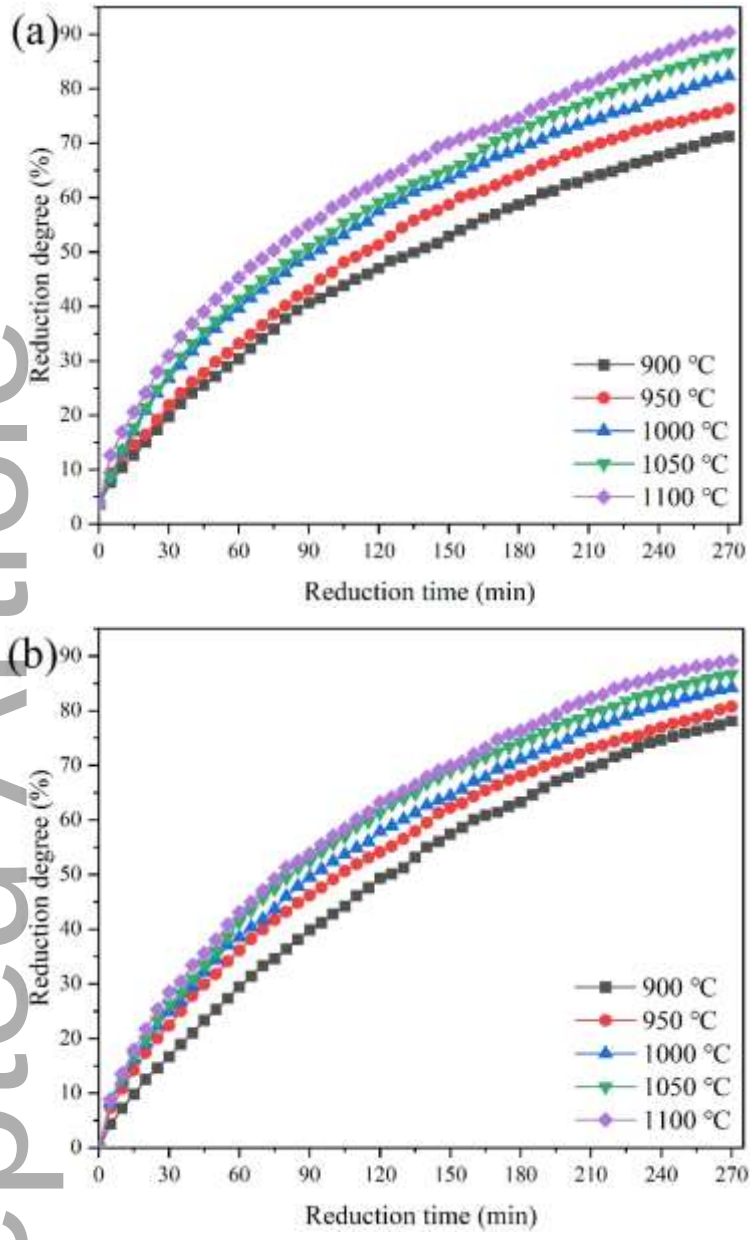

Fig. 3 Reduction kinetic curves of CBB (a) and CBBC (b)

To compare the reduction velocity of CBB and CBBC, the reduction velocity index (RVI) was employed to evaluate the reduction behavior of CBB and CBBC. The RVI equation refers to the standards of ISO 4695-1995 and is given below as Eq. (23):[37]

$$\mathrm{RVI} = dR_t/d_t = 33.6/(t_{60} - t_{30}) \quad (23)$$

where t_{30} is the reduction time to reach 30% of the reduction degree, min; t_{60} is the reduction time to reach 60% of the reduction degree, min; and 33.6 is a constant.

The RVI of CBB and CBBC at different temperatures is shown in Figure 4. At the same temperature, CBBC has a higher RVI value than CBB. At high temperatures, CBB and CBBC has a higher RVI value compared to low temperatures. One of the reasons CBBC has a larger RVI could be that the carbon in CBBC experiences a gasification reaction, which increases the atmosphere's CO concentration more than that of CBB and accelerates the reduction reaction. In reducing the off gas of the CBB and CBBC samples throughout the reduction process, the off gas type and change trend of the CO/CO_2 ratio may be consistent, indicating that the off gases present include CO, CO_2, and N_2, the CO/CO_2 ratio increase steadily during the reduction process[38-40].

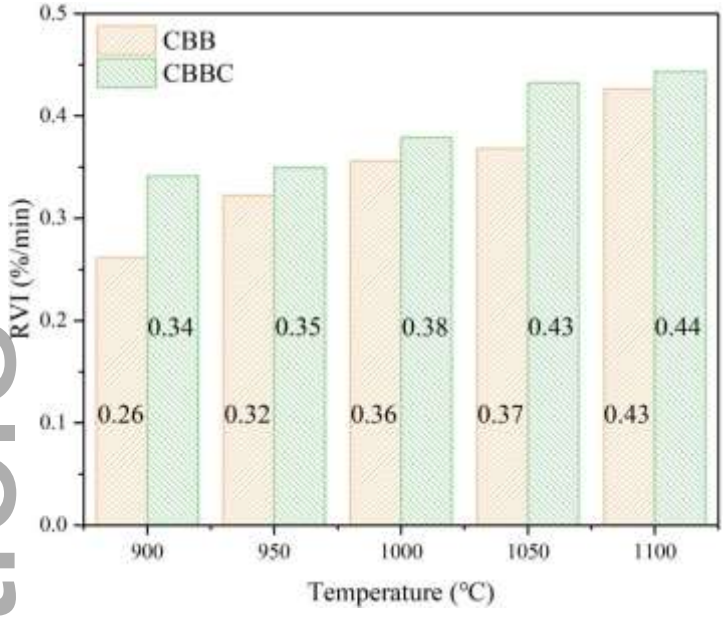

Fig. 4 Reduction velocity index (RVI) of CBB and CBBC at different temperatures

3.2 Reduction kinetics analysis

3.2.1 Kinetics analysis of CBB

3.2.1.1 Rate-controlling step

Figure 5 shows the results of fitting the rate-controlling step models to the CBB experimental data. The plots of $1-(1-R)^{1/3}$ vs. time of interfacial chemical reaction model according to Eq. (6) are shown in Figure 5 (a). As demonstrated, the reduction process is controlled by the interfacial chemical reaction since the relationship between $1-(1-R)^{1/3}$ and time t are essentially linear at the early stage of the reaction. However, there are deviations as the reduction process continues, thus the kinetic data are fitted with both the internal diffusion and the interfacial chemical reaction model. The plots of 1-t/F vs. $3F-2F^2$ of both interfacial chemical reaction and internal diffusion model according to Eq. (7) are shown in Figure 5 (b), it is clear that the reduction process is controlled by the both interfacial chemical reaction and internal diffusion model since the relationship between t/F and $3F-2F^2$ are essentially linear. The reaction rate constant k and diffusion coefficient De are obtained by Eq. (13) and Eq. (14), respectively. However, there are deviations of 1000 ℃, 1050 ℃ and 1100 ℃ as the reduction process goes into the final stage, thus the data are fitted with an internal diffusion model for the final stage. The plots of $1-3(1-R)^{2/3}+2(1-R)$ vs. time of internal diffusion model according to Eq. (15) are shown in Figure 5 (c). The figure shows that the reduction process is controlled by the internal diffusion model in the final stage since the relationship between $1-3(1-R)^{2/3}+2(1-R)$ and time t are essentially linear. In general, with the increase of temperature, the time range of interfacial chemical reaction model as a rate-controlling step is shortened, the start time of both interfacial chemical reaction and internal diffusion models is advanced as a rate-controlling step, and the time range of the internal diffusion model as a rate-controlling step is expanded.

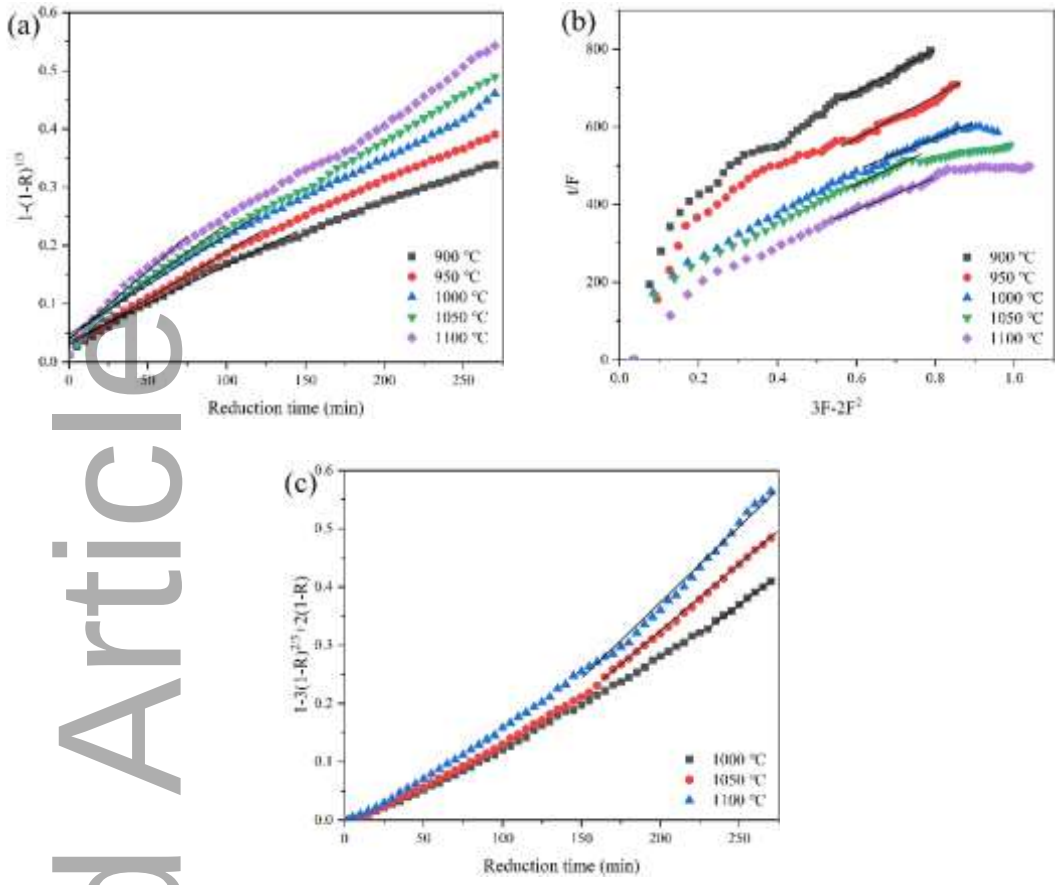

Fig. 5 Results of fitting rate-controlling step models to the CBB experimental data: (a) interfacial chemical reaction model, (b) both interfacial chemical reaction and internal diffusion model and (c) internal diffusion model.

Table 5 summarizes the time range of the rate-controlling steps, the reaction rate constant and the diffusion coefficient. When the rate-controlling step is an interfacial chemical reaction, the reaction rate constant increases as the temperature increases. When the rate-controlling step is both interfacial chemical reaction and internal diffusion, the reaction rate constant and diffusion coefficient increase with as the temperature increases. When the rate-controlling step is internal diffusion, the diffusion coefficient increases as the temperature increase.

Table 5 Reaction rate constants and effective diffusion coefficients for CBB

Rate-controlling step	Temperature (°C)	900	950	1000	1050	1100
Interfacial chemical reaction	Time range (min)	0-145	0-125	0-120	0-100	0-75
	$k(10^{-3}m/s)$	4.41	5.26	6.16	6.98	8.54
	R at the end (%)	51.72	52.82	57.47	53.41	50.13
Both interfacial chemical reaction and internal diffusion	Time range (min)	145-270	125-270	120-230	100-160	75-160
	$k(10^{-4}m/s)$	4.01	5.81	7.96	9.90	11.60
	$De(10^{-6}m^2/s)$	1.68	1.79	1.93	2.12	2.37

	R at the end (%)	71.16	76.32	76.24	67.50	71.85
	Time range (min)			230-270	160-270	160-270
Internal diffusion	De($10^{-6}m^2/s$)			1.86	2.15	2.66
	R at the end (%)			82.37	86.70	90.43

3.2.1.2 Apparent activation energy

According to Eq. (21), the plot of lnk vs. 1/T would yields a straight line and from the slopes the apparent activation energy (Ea) can be evaluated, the plot of lnk vs. 1/T is shown in Figure 6. Based on the results of Figure 6, the apparent activation energies of interfacial chemical reaction model (Figure 6a), both interfacial chemical reaction model and internal diffusion model (Figure 6b and 6c) and internal diffusion model (Figure 6d) are 46.20 kJ/mol, 56.74 kJ/mol, 38.24 kJ/mol and 40.74 kJ/mol, respectively, which can be seen in Table 6.

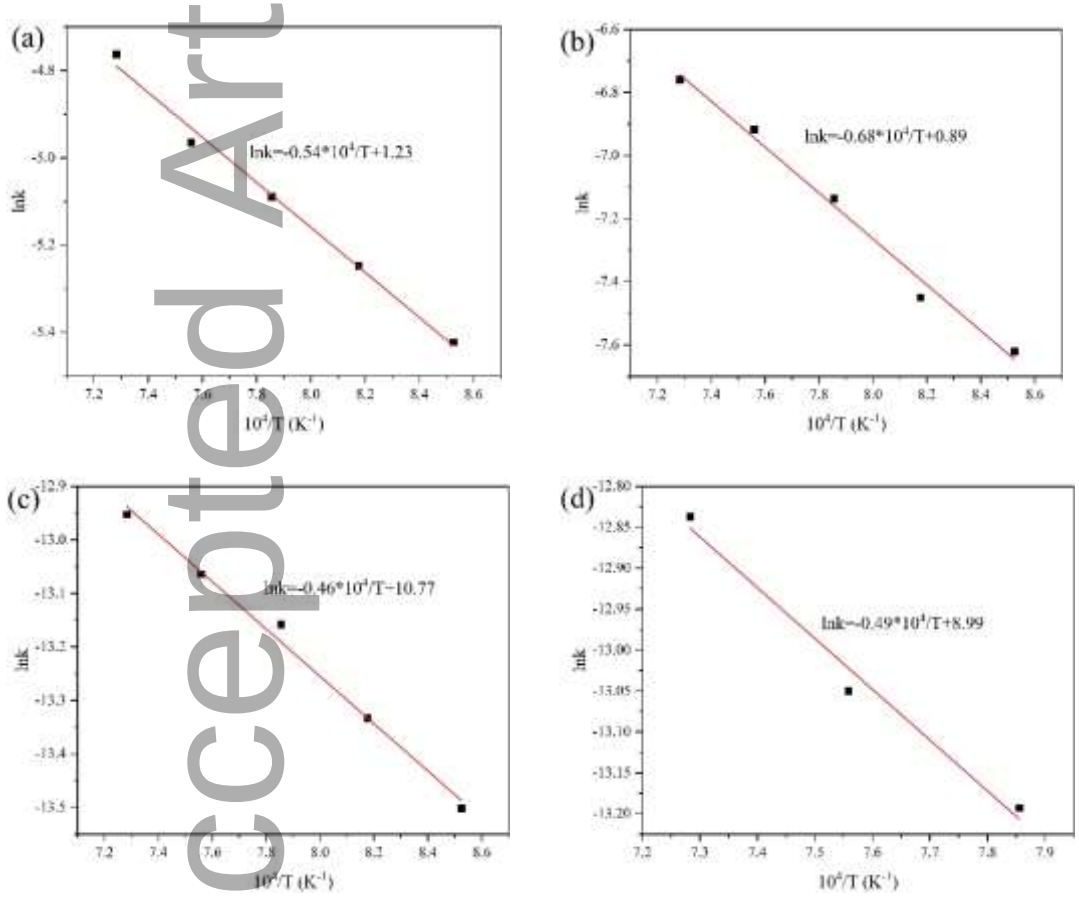

Fig. 6 Arrhenius plots of the CBB kinetic reaction: (a) interfacial chemical reaction model, (b) both interfacial chemical reaction and internal diffusion model (fitting based on reaction rate constants) (c) both interfacial chemical reaction and internal diffusion model (fitting based on effective diffusion coefficients) and (d) internal diffusion model.

Table 6 Activation energies of CBB under different rate-controlling steps

Rate-controlling step	Interfacial chemical reaction	Both interfacial chemical reaction and internal diffusion	Internal diffusion

		Interfacial chemical reaction	Internal diffusion	
Apparent activation energy, Ea (kJ/mol)	46.20	56.74	38.24	40.74

Figure 7 shows a comparison of the apparent activation energy for CBB determined using the model-fitting method and the Friedman method. The apparent activation energy for CBB was determined using Eq. (22), and as demonstrated, each apparent activation energy determined by the model-fitting method falls within the range of apparent activation energies determined by the Friedman method, which suggests that the model fitting for the apparent activation energy result is reasonable. Similar types of apparent activation energy values were observed by Wang et al. 44.12 kJ/mol for Fe_2O_3 powder[41] and Liu et al. 48.64 kJ/mol for iron oxide briquettes[42].

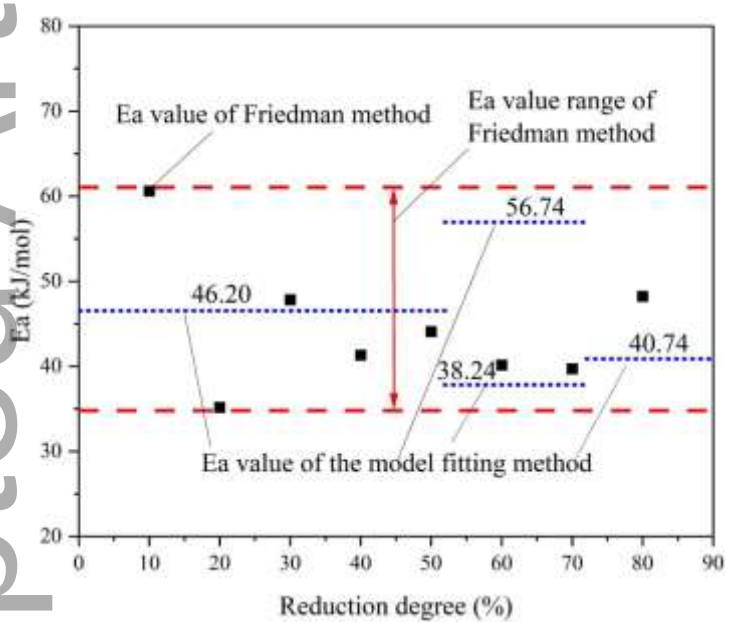

Fig. 7 Comparison of the apparent activation energy for CBB determined using the model-fitting and Friedman methods.

3.2.2 Kinetics analysis of CBBC

3.2.2.1 Rate-controlling step

Figure 8 shows the results of fitting the rate-controlling step models to the CBBC experimental data. The plots of -ln(1-α) vs. time of the gasification of carbon reaction model according to Eq. (16) are shown in Figure 8 (a). As demonstrated, the relationship between -ln(1-α) and time t is essentially linear during the whole reduction process. The plots of 1-$(1-\alpha)^{1/3}$ vs. time of the interfacial chemical reaction model according to Eq. (17) are shown in Figure 8 (b), it is clear that the relationship between 1-$(1-\alpha)^{1/3}$ and time is essentially linear. The plots of $[1-(1-\alpha)^{1/3}]^2$ vs. time of the internal diffusion model according to Eq. (18) are shown in Figure 8 (c), the overall fitting result is not good because $[1-(1-\alpha)^{1/3}]^2$ does not exhibit a linear relationship with time in the early stages of the reduction process but does so in the later stages.

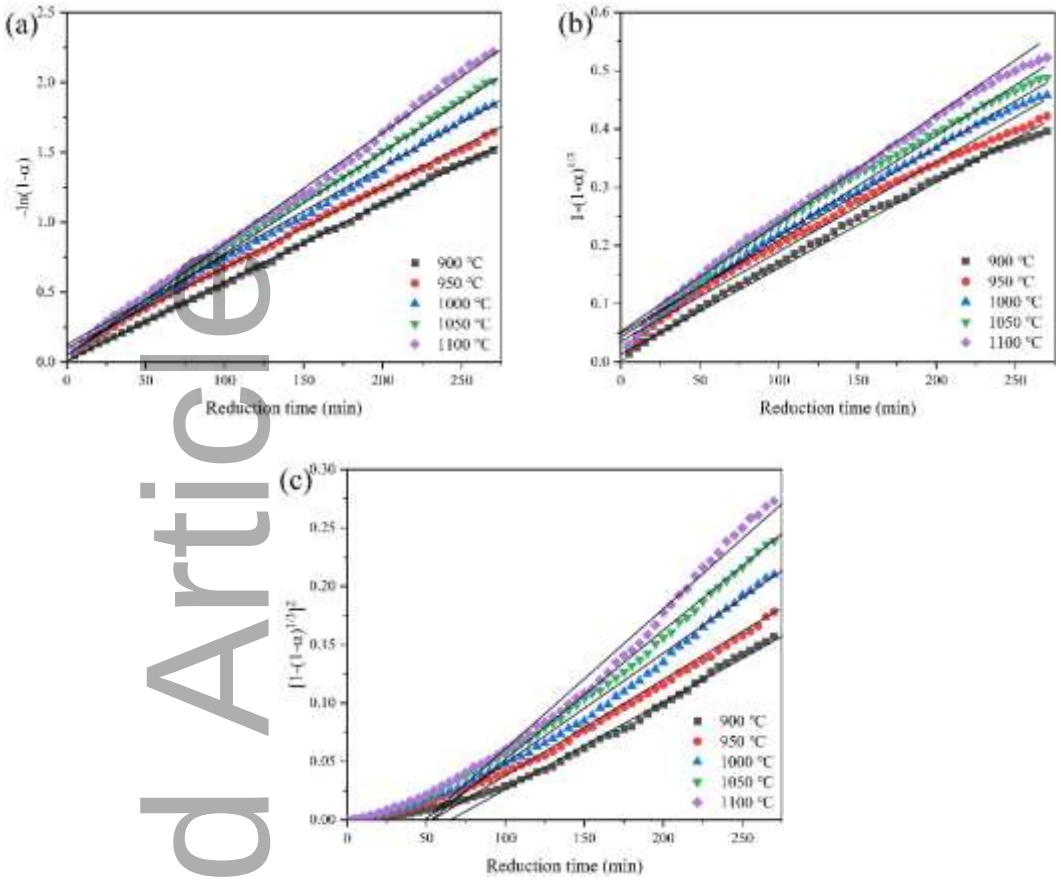

Fig. 8 Results of fitting rate-controlling step models to the CBBC experimental data: (a) gasification of carbon reaction model, (b) interfacial chemical reaction model and (c) internal diffusion model.

To accurately assess the rate-controlling steps, the reaction rate constants (k), correlation coefficients (R^2), MD and RMSD of the three models are summarized, as shown in Table 7. Compared with those of other models, the R^2 of the gasification of carbon reaction model is bigger, and the MD and RMSD are smaller; the R^2, MD and RMSD of the interfacial chemical reaction model are closer to those of the carbon gasification reaction model; the R^2 of the internal diffusion model is smaller and the MD and RMSD are bigger than those of other models. As a result, it is determined that the gasification of carbon reaction or interfacial chemical reaction is the rate-controlling step.

Table 7 Reaction rate constants, correlation coefficient, MD, and RMSD for CBBC

Rate-controlling step	Temperature (℃)	900	950	1000	1050	1100
Gasification of carbon reaction	k(10^{-5}m/s)	9.37	9.68	10.93	12.05	13.23
	R^2	0.9995	0.9985	0.9989	0.9987	0.9976
	MD	-0.0042	-0.0404	-0.0348	-0.0287	-0.0241

	RMSD	0.0073	0.0450	0.0404	0.0342	0.0321
	k(10^{-5}m/s)	2.43	2.48	2.67	2.87	3.05
Interfacial chemical reaction	R^2	0.9964	0.9891	0.9921	0.9869	0.9928
	MD	-0.0384	-0.0775	-0.0826	-0.0831	-0.0834
	RMSD	0.0416	0.0844	0.0894	0.0921	0.0918
	k(10^{-5}m/s)	1.03	1.14	1.35	1.54	1.77
	R^2	0.9643	0.9810	0.9750	0.9811	0.9711
Internal diffusion	MD	0.1017	0.0760	0.0802	0.0816	0.0880
	RMSD	0.1200	0.0896	0.0952	0.0992	0.1053

3.2.2.2 Apparent activation energy

According to Eq. (21), the plot of lnk vs. 1/T is presented in Figure 9, and from the slopes, the activation energy (Ea) is calculated. Based on the findings of Figure 9, the apparent activation energies of the gasification of carbon reaction model (Figure 9 (a)) and interfacial chemical reaction model (Figure 9 (b)) are 32.42 kJ/mol, and 18.29 kJ/mol, respectively, as shown in Table 8.

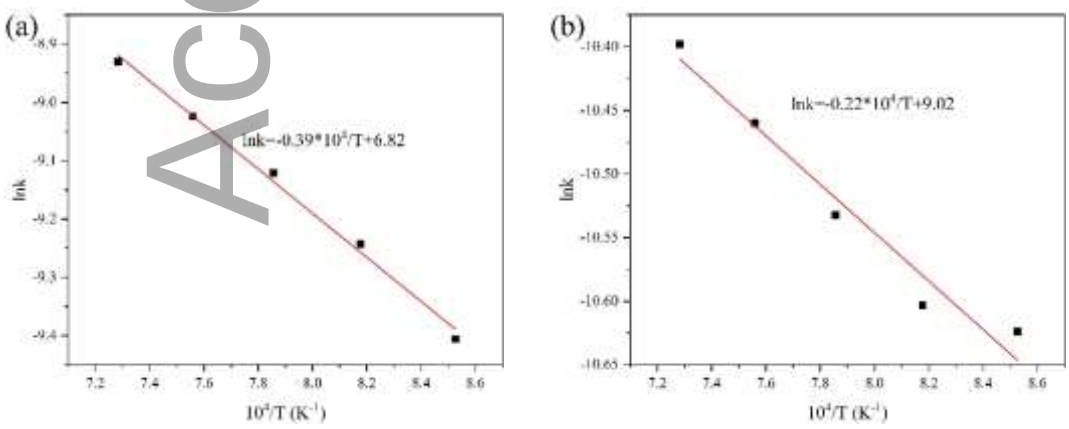

Fig. 9 Arrhenius plots of the CBBC kinetic reaction: (a) the gasification of carbon reaction model and (b) the interfacial chemical reaction model.

Table 8 Activation energies of CBBC under different rate-controlling step

Rate-controlling step	Carbon gasification reaction	Interfacial chemical reaction
Apparent activation energy, Ea (kJ/mol)	32.42	18.29

Figure 10 shows a comparison of the apparent activation energy for CBBC determined using the model-fitting method and the Friedman method. It is determined that the carbon gasification reaction is a rate-controlling step in the CBBC reduction process since the apparent activation energy obtained from the carbon gasification reaction model is within the range of the apparent activation energy acquired from the Friedman method. Similar types of apparent activation energy values were found by Sah et al. 12.37-38.32 kJ/mol for iron ore-coal composite pellet[43] and Raj et al. 20.87-31.92 kJ/mol for highly fluxed iron ore pellets[44].

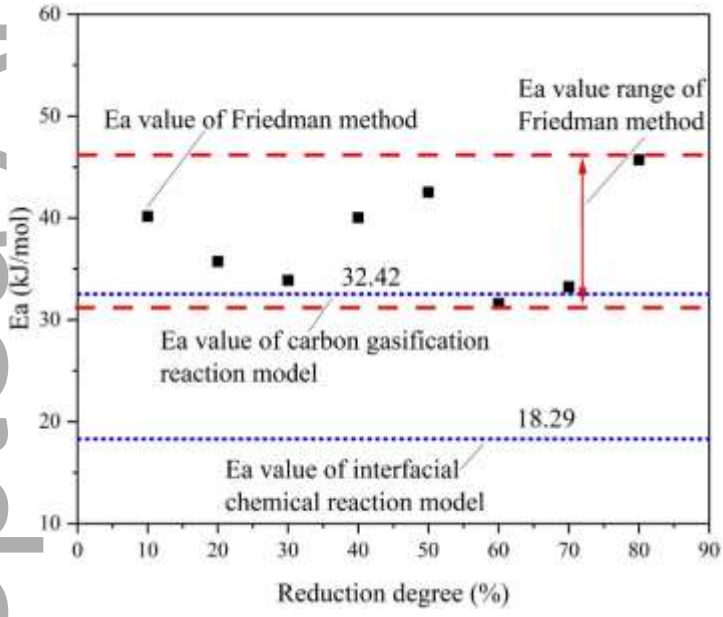

Fig. 10 Comparison of the activation energy for CBBC determined using the Friedman method and the model of rate-controlling steps.

3.3 Phase transformation and morphology analysis

In order to further study the reasons for the difference in reduction kinetics between CBB and CBBC, compressive strength, phase transformation and microstructure were examined. Figure 11 illustrate the compressive strength of the CBB and CBBC before and after reduction experiment, the compressive strength decreased significantly after reduction. At 950 °C, the compressive strength is at its lowest value, it then increases as the reduction temperature increases. This is due to the reduced iron start sintering, which helps to enhance compressive strength[45].

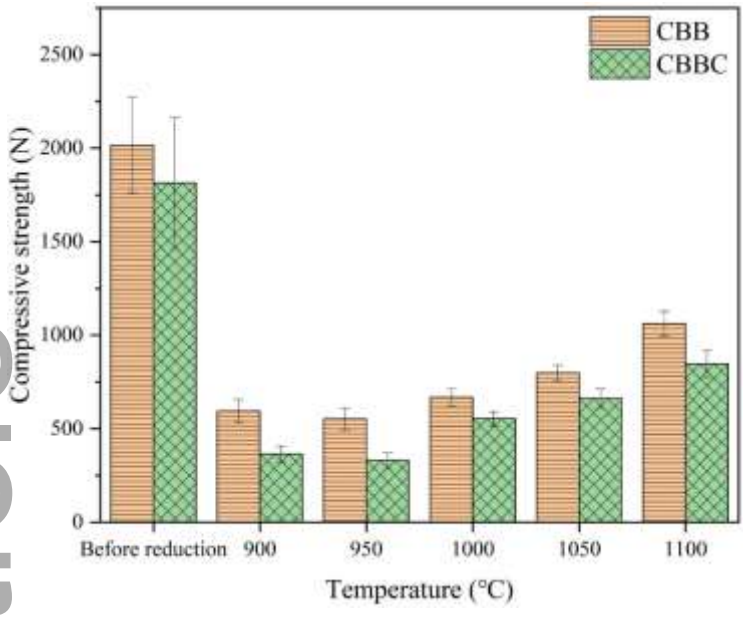

Fig. 11 Compressive strength of the samples before and after reduction experiment.

The XRD patterns of the reduction products at different temperatures are shown in Figure 12. Figure 12 (a) shows the XRD pattern of the periphery and core parts of CBB's reduction products, at 900 °C, the main phases of the periphery part are metallic iron, wüstite and silicate, while the main phases of the core part are calcium ferrite, wüstite and silicate. At 950 °C and above, metallic iron and silicate are the main phases of the periphery part, and metallic iron, wüstite, silicate and calcium ferrite are the main phases of the core part. The intensity of the metallic iron peak (2θ=44.80°) increases with the increase in temperature, which indicates that the increase in temperature promotes the metallic iron formation. Figure 12 (b) shows the XRD pattern of periphery and core parts of CBBC's reduction products; at 900 °C, the main phases of the periphery part are metallic iron, wüstite and silicate, while the main phases of the core part are metallic iron, wüstite, silicate and calcium ferrite. At 950 °C and above, metallic iron and silicate are the main phases of the periphery part. At 950 °C, 1000 °C, and 1050 °C, the core part is mainly composed of metallic iron, wüstite, silicate and calcium ferrite, whereas at 1100 °C, it is primarily composed of metallic iron, silicate and calcium ferrite. With the increase in temperature, the wüstite peak weakens, which indicates that the reduction degree is improving. By combining Figures 12 (a) and (b), we can conclude that coke promotes the phase transformation in CBBC. These results support the findings in Section 3.2, which indicate that the apparent activation energy of the CBBC interfacial chemical reaction model is lower than the apparent activation energy of CBB.[37, 46] Lower apparent activation energies are more favorable for reduction reactions.

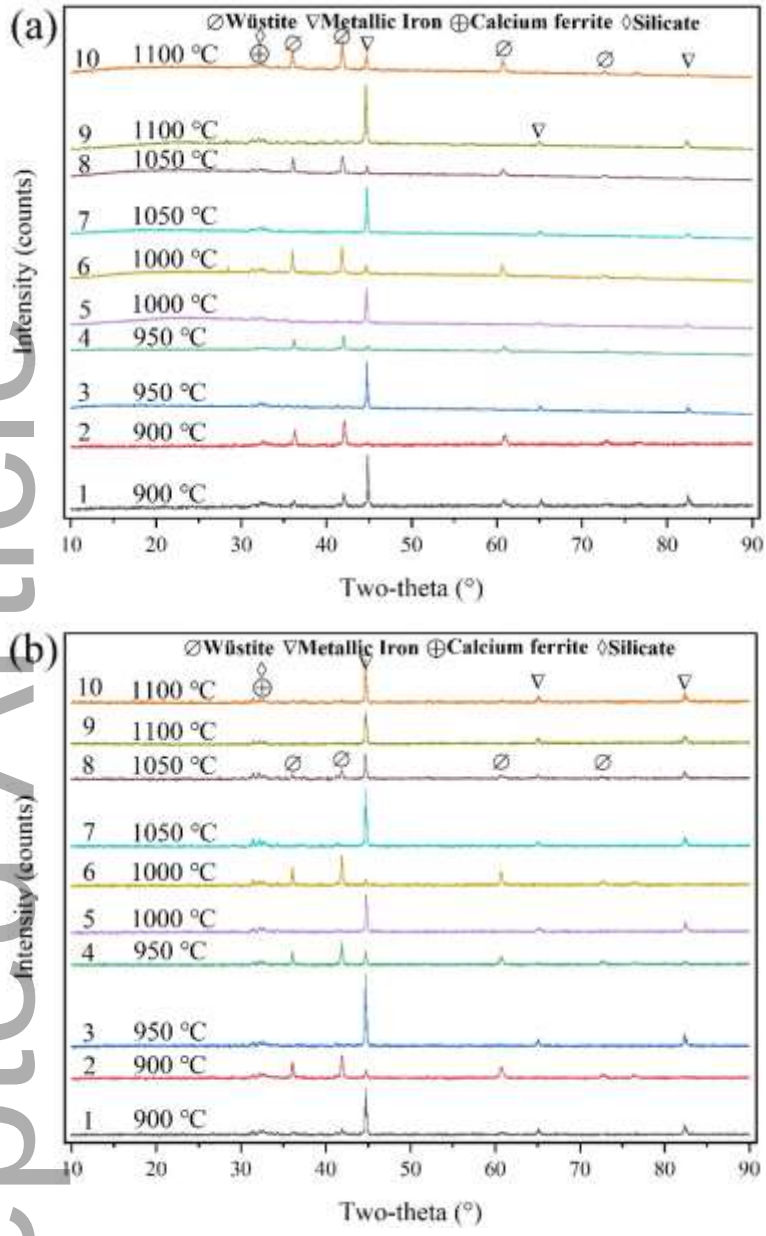

Fig. 12 XRD patterns of reduction products: (a) XRD patterns No. 1, 3, 5, 7, and 9 are the CBB's periphery parts; No. 2, 4, 6, 8, and 10 are the CBB's core part. (b) XRD patterns No.1, 3, 5, 7, and 9 are the CBBC's periphery part; No. 2, 4, 6, 8, and 10 are the CBBC's core part.

SEM images of the reduction products of CBB's periphery and core parts at different temperatures are shown in Figure 13. At 900 °C, the iron bearing phases are again different colors from the periphery part. As the temperature increases, the amount of white metallic iron phases exhibits an increase in the peripheral part. In the reduction products of the core parts, the iron bearing phases have sharp edges and corners at 900 °C (blue dashed lines mark some of them), and then become smooth with the increase in temperature. However, at 1100 °C, the iron bearing phase is still embedded with the metallic iron phase and has clear borders and corners (blue dashed lines mark some of them).

SEM images of the reduction products of CBBC's periphery and core parts at different temperatures are shown in Figure 14. Compared with the periphery part, white metallic iron phase is present at 900 °C, and when the temperature increases, the amount of white metallic iron phase continues to increase. The comparison of the core part reveals that at 900 °C, the iron bearing phase's edges and corners are blurry (blue dashed lines mark some of them), and as the temperature increases, they become smoother. At 1100 °C, the adjacent metallic iron phases are

connected, and only a few iron bearing phases are embedded in the metallic iron phase (blue dashed lines mark some of them). The temperature, atmosphere and sintering phenomenon are the reasons why the edges and corners are smooth.[47] The smoother edges and corners of CBBC are achieved by coke reduction since the reduction temperature and sintering phenomenon are the same as those of CBB. This suggests that the CBBC sample is more thoroughly reduced than the CBB sample, which is consistent with the results of Figure 12. The results in Figure 13 and 14 show that metallic iron phase appears in the core part at temperatures of 950 °C and above, which indicates that increasing the temperature promotes the reduction reaction of the sample.

Temperature	Periphery part	Core part
900 ℃	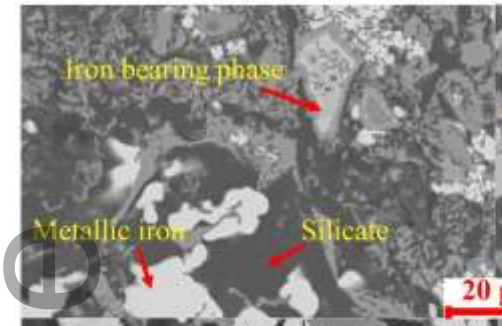	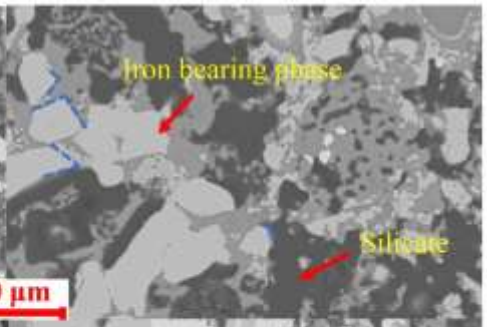
950 ℃	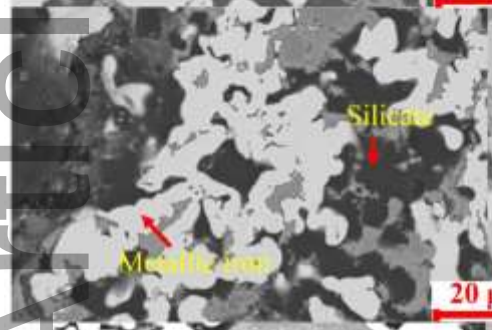	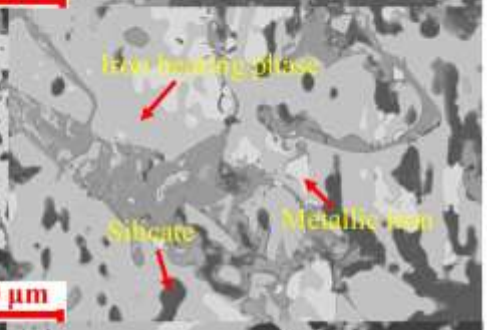
1000 ℃	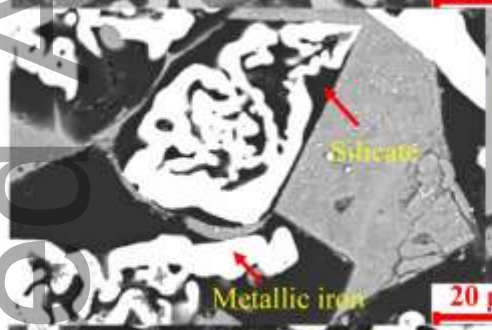	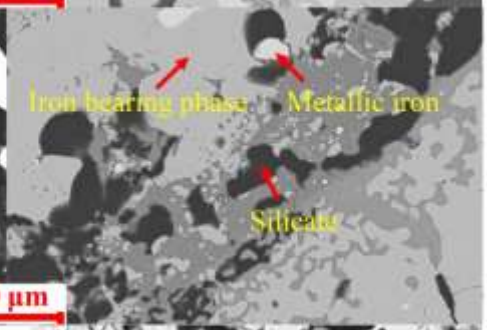
1050 ℃	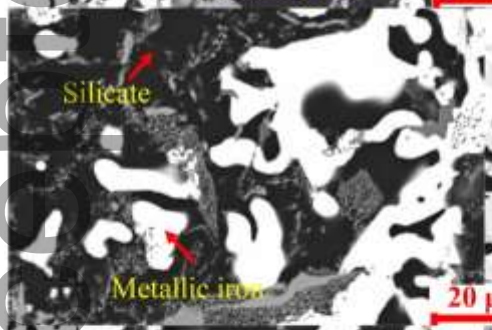	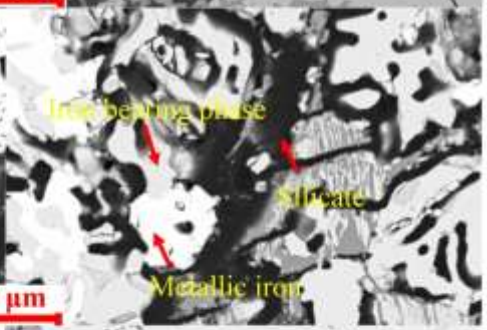
1100 ℃	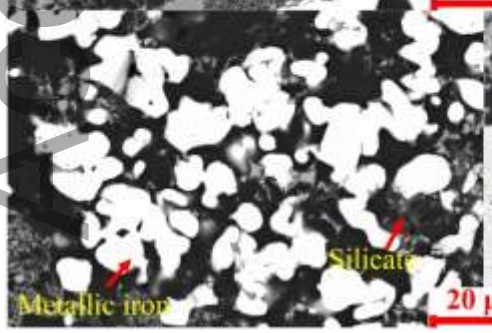	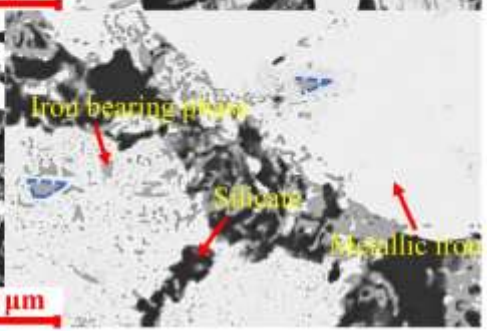

Fig. 13 SEM images of CBB reduction products at different temperatures and parts of briquette.

Temperature	Periphery part	Core part

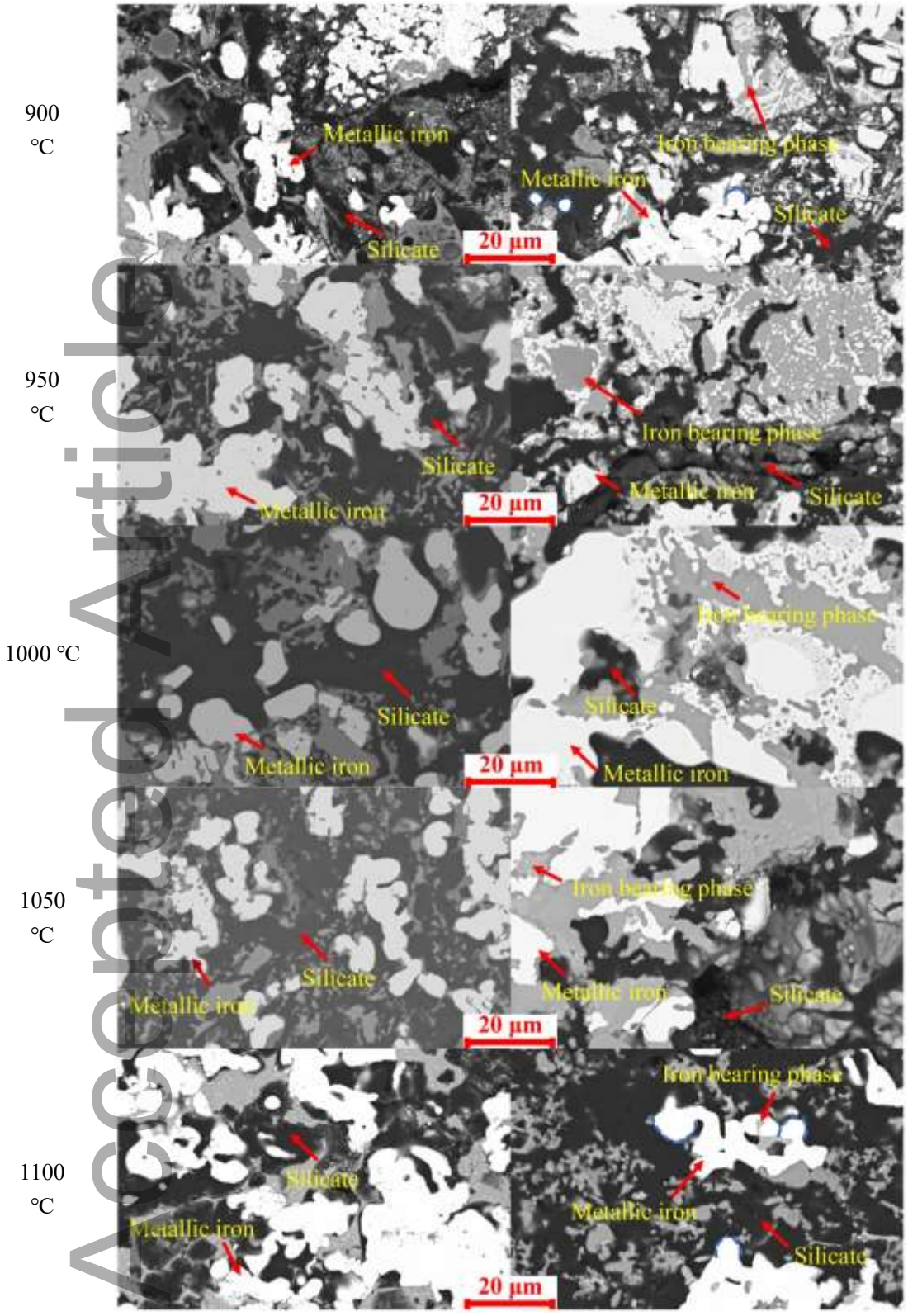

Fig. 14 SEM images of CBBC reduction products at different temperatures and parts of briquette.

4. Conclusions

The reduction kinetics of two types of cold-bonded briquette prepared from return fines of sinter with carbon

monoxide and coke were studied. One type was CBB, and the other was CBBC. The main conclusion and key findings are summarized as follows:

1. The reduction temperature obviously impacts the reduction degree of CBB and CBBC. CBBC has a higher RVI value than CBB at the same temperature. Both CBB and CBBC have a larger value of reduction velocity index at high temperatures than at low temperatures.

2. The reduction kinetics of CBB were evaluated using a core-shrinking model. The early stages of the CBB reduction process at 900 and 950 °C are controlled by interfacial chemical reaction, followed by both interfacial chemical reaction and internal diffusion. The early stages of the CBB reduction process are controlled by a chemical reaction at 1000, 1050, and 1100 °C, then by both interfacial chemical reaction and internal diffusion; the later stages are controlled by internal diffusion. The apparent activation energy of the interfacial chemical reaction is 46.20 kJ/mol; however, the apparent activation energies of both interfacial chemical reaction and internal diffusion are 56.74 kJ/mol and 38.24 kJ/mol for interfacial chemical reaction and gas internal diffusion, respectively; the apparent activation energy of the internal diffusion is 40.74 kJ/mol. According to the calculation results of the Friedman method, the apparent activation energy of CBB determined by the model-fitting method is reasonable.

3. The kinetics analysis of CBBC indicates that, the reduction process is controlled by the gasification reaction of carbon. The apparent activation energy of the interfacial chemical reaction is 32.42 kJ/mol. According to the calculation results of the Friedman method, the apparent activation energy of CBBC determined by the model-fitting method is reasonable.

4. By comparing the XRD patterns of CBB and CBBC samples, it was found that coke promotes the phase transformation in CBBC. SEM results indicate that the iron bearing phase, or metallic iron phase of the CBBC sample had smoother edges and corners than the CBB sample, which indicates that the CBBC sample was more thoroughly reduced than the CBB sample.

Acknowledgements

This work was supported by China Scholarship Council under grant No. (202106890046), the National Natural Science Foundation of China under grant No. (51974182), Program for Professor of Special Appointment (Eastern Scholar) at Shanghai Institutions of Higher Learning under grant No. (TP2015039), National 111 Project (The Program of Introducing Talents of Discipline to University), under grant No. (D17002), Independent Research Project of State Key Laboratory of Advanced Special Steel, Shanghai Key Laboratory of advanced Ferrometallurgy, Shanghai University (SKLASS 2022-Z01) and the Science and Technology Commission of Shanghai Municipality, under grant No.(19DZ2270200), and China Baowu Low Carbon Metallurgy Innovation Foudation-BWLCF202112. The authors thank Mr. Tommi Kokkonen and Mr. Riku Mattila for their help with the experimental work.

Conflict of interest

On behalf of all authors, the corresponding author states that there is no conflict of interest.

References

[1] Y. Li, Y. Cao, H. Nie, S. Wei, L. Yan, Y. Yu, *China Metall.* **2022**, *32*, 21.

[2] Y. Li, H. Chen, A. Hammam, H. Wei, H. Nie, W. Ding, M. Omran, L. Yan, Y. Yu, *Materials* **2021**, *14*, 1.
[3] Y. Li, Y. Zang, Y. Xiong, D. Qiu, C. Wang, L. Yan, Y. Yu, *Metall. Mater. Trans. B* **2023**, *54*, 355.
[4] Y. Li, Y. Xiong, Y. Zang, H. Chen, L. Yan, Y. Yu, *Steel Res. Int.* **2022**, *93*, 2200304.
[5] D. Spreitzer, J. Schenk, *Steel Res. Int.* **2019**, *90*, 1.
[6] K. Higuchi, R. H. Heerema, *ISIJ Int.* **2005**, *45*, 574.
[7] N. Sakamoto, H. Noda, K. Ichikawa, H. Sato, H. Kawata, *ISIJ Int.* **1997**, *37*, 1066.
[8] R. Corbari, R. J. Fruehan, *Metall. Mater. Trans. B* **2010**, *41*, 318.
[9] M. Matsumura, M. Hoshi, T. Kawaguchi, *ISIJ Int.* **2005**, *45*, 594.
[10] J. O. Edstrom, *J. Iron Steel Inst., London* **1953**, *175*, 289.
[11] Z. Liang, Ironmaking science, Metallurgical Industry Press, Beijing, BJ **2009**.
[12] W. Tang, S. Yang, L. Zhang, Z. Huang, H. Yang, X. Xue, *J. Cent. South Univ. (Engl. Ed.)* **2019**, *26*, 132.
[13] E. A. Mousa, *Ironmaking Steelmaking* **2014**, *41*, 418.
[14] Z. Yu, G. Li, T. Jiang, Y. Zhang, F. Zhou, Z. Peng, *ISIJ Int.* **2015**, *55*, 907.
[15] T. Umadevi, A. Brahmacharyulu, R. Sah, *Ironmaking Steelmaking* **2014**, *41*, 270.
[16] M. M. Hessien, Y. Kashiwaya, K. Ishii, M. I. Nasr, A. A. El-Geassy, *Ironmaking Steelmaking* **2008**, *35*, 191.
[17] S. Yang, M. Zhou, X. Xue, T. Jiang, C. Sun, *JOM* **2019**, *71*, 2812.
[18] W. Li, G. Fu, M. Chu, M. Zhu, *Steel Res. Int.* **2017**, *88*, 1600228.
[19] S. Mishra, G. G. Roy, *Metall. Mater. Trans. B* **2016**, *47*, 2347.
[20] X. Ma, M. Jiang, Q. Wang, X. Wang, *J. Northeast. Univ., Nat. Sci.* **2002**, *23*, 440.
[21] A. V. Bradshaw, A. G. Matyas, *Metall. Mater. Trans. B* **1976**, *7*, 81.
[22] M. I. Nasr, A. A. Omar, M. H. Khedr, A. A. El-Geassy, *ISIJ Int.* **1995**, *35*, 1043.
[23] I. V. Flores, O. Matos, A. L. da Silva, M. C. Bagatini, *Metall. Mater. Trans. B* **2021**, *52*,1716.
[24] S. Yang, M. Zhou, T. Jiang, X. Xue, *Int. J. Miner., Metall. Mater.* **2018**, *25*, 145.
[25] Y. Sui, Y. Guo, T. Jiang, G. Qiu, *J. Alloys Compd.* **2017**, *706*, 546.
[26] X. Huang, Principles of iron and steel metallurgy, Metallurgical Industry Press, Beijing, BJ **2013**.
[27] Y. Man, J. Feng, F. Li, Q. Ge, Y. Chen, J. Zhou, *Powder Technol.* **2014**, *256*, 361.
[28] H. Long, J. Li, P. Wang, S. Shi, *Ironmaking Steelmaking* **2012**, *39*, 585.
[29] C. E. Seaton, J. S. Foster, J. Velasco, *Trans. Iron Steel Inst. Jpn.* **1983**, *23*, 490.
[30] W. Jander, Z. Anorg. Allg. Chem. **1927**, *163*, 1.
[31] Y. K. Rao, *Metall. Trans.* **1971**, *2*, 1439.
[32] J. D. Hancock, J. H. Sharp, *J. Am. Ceram. Soc.* **1972**, *55*, 74.
[33] K. Piotrowski, K. Mondal, H. Lorethova, L. Stonawski, T. Szymański, T. Wiltowski, *Int. J. Hydrogen Energy* **2005**, *30*, 1543.
[34] H. L. Friedman, *J. Polym. Sci., Part C: Polym. Symp.* **1964**, *6*, 183.
[35] B. F. d'Arlas, L. Rueda, P. M. Stefani, K. de la Caba, I. Mondragon, A. Eceiza, *Thermochim. Acta* **2007**, *459*, 94.
[36] Q. Shu, J. L. Klug, Q. Li, *ISIJ Int.* **2019**, *59*, 1057.
[37] D. Guo, Y. Li, B. Cui, Z. Chen, S. Luo, B. Xiao, H. Zhu, M. Zhu, *Chem. Eng. J.* **2017**, *327*, 822.
[38] H. Park, V. Sahajwalla, *ISIJ Int.* **2014**, *54*, 49.
[39] R. J. De Carvalho, P. G. Quariguasi Netto, J. C. D'abreu, *Can. Metall. Q.* **1994**, *33*, 217.
[40] N. S. Srinivasan, A. K. Lahiri, *Metall. Mater. Trans. B* **1977**, *8*, 175.
[41] Y. D. Wang, X. N. Hua, C. C. Zhao, T. T. Fu, W. Li, W. Wang, *Int. J. Hydrogen Energy* **2017**, *42*, 5667.
[42] D. Liu, X. Wang, J. Zhang, Z. Liu, K. Jiao, X. Liu, R. Wang, *Metall. Res. Technol.* **2017**, *114*, 611.
[43] R. Sah, S. K. Dutta, *Trans. Indian Inst. Met.* **2011**, *64*, 583.
[44] R. K. Dishwar, O. P. Sinha, *Fuel* **2021**, *296*, 1.
[45] C. Takano, M. B. Mourao, *ISIJ Int.* **2001**, *41*, S22.
[46] D. Guo, M. Hu, C. Pu, B. Xiao, Z. Hu, S. Liu, X. Wang, X. Zhu, *Int. J. Hydrogen Energy* **2015**, *40*, 4733.

[47] P. Garg, X. Hu, Y. Li, K. Li, S. Nag, J. Zhang, *Metall. Mater. Trans. B* **2022**, *53*, 1759.

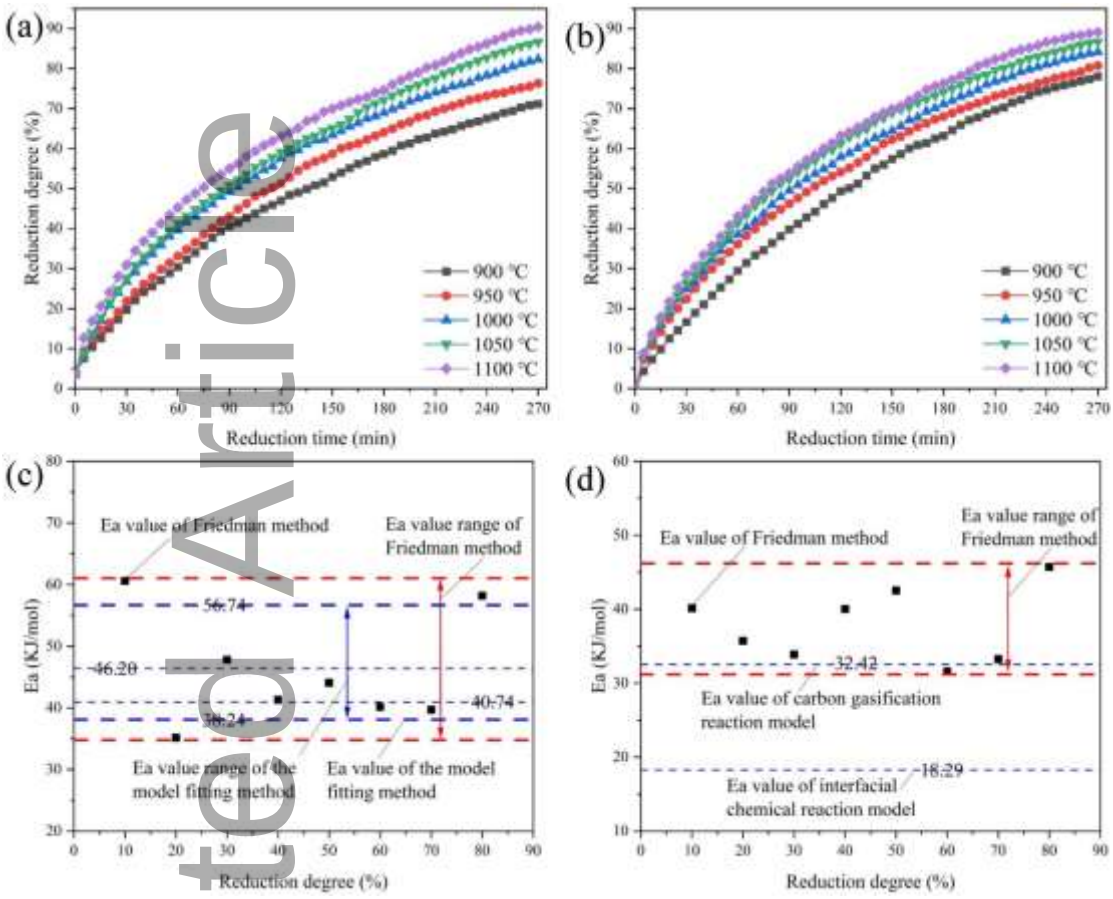

Reduction kinetic of cold-bonded briquettes without coke (CBB) and with coke (CBBC) is presented. Figure (a) and (b) illustrate the reduction kinetic curves of CBB and CBBC. Figure (c) and (d) illustrate the comparison of the apparent activation energy for CBB and CBBC determined using the model fitting method and Friedman method.